

Observational Characteristics of the First Protostellar Cores

Kazuuyuki OMUKAI

National Astronomical Observatory, Mitaka, Tokyo 181-8588, Japan; omukai@th.nao.ac.jp

(Received 2006 January 1; accepted 2006 January 1)

Abstract

First protostellar cores are young stellar objects in the earliest evolutionary stage. They are hydrostatic objects formed soon after the central portions of star-forming cores become optically thick to dust emission. We consider their characteristics in the emitted radiation, and discuss their evolution with increasing mass of the cores. Particular attention is paid to detailed radiative and chemical processes in the postshock relaxation layer located at the surface of the core, where the majority of radiation is emitted. Most of the radiation is originally emitted in the dust continuum in mid-infrared wavelength ($\sim 10 - 30\mu\text{m}$), which reprocessed to far-infrared with $\sim 100 - 200\mu\text{m}$. Although some fraction (~ 0.1) of the radiation energy is emitted in the H_2O lines at the accretion shock, most is absorbed and reemitted in the dust continuum in the envelope. The H_2O lines account for at most $\sim 1/100$ of the observed luminosity. If a cavity is present in the envelope due to outflow or rotation, the dust and H_2O line emission in the mid-infrared wavelength from the shock can be observed directly, or as a reflection nebula. Among forthcoming observational facilities, *SPICA Infrared telescope for Cosmology and Astrophysics (SPICA)* is the most suitable for detecting either direct or processed radiation from first-core objects.

Key words: ISM: clouds — ISM: molecules — stars: formation — stars: pre-main-sequence

1. Introduction

Evolution from the collapse of dense molecular cores to the formation of protostars has been discussed theoretically for several decades (e.g., Hayashi 1966; Shu, Adams, & Lizano 1987). Advances in radio and infrared observations have confirmed many aspects of the evolution. The earliest phase of protostellar evolution, i.e., the first core, however, still eludes observational confirmation though a theoretical prediction was made almost forty years ago (Larson 1969). A first core is a hydrostatic object that forms after a star-forming core becomes optically thick to the dust continuum and the temperature evolution becomes adiabatic owing to inefficient radiative cooling. Their roles in protostellar evolution include enabling binary formation and/or driving protostellar outflow (e.g., Inutsuka 2004). The difficulty in finding first-core objects is due to the following reasons. First, first-core objects are short-lived. After formation, they grow in mass by accretion of the envelope matter and the temperature inside increases. When the mass of the first core reaches about $0.05M_\odot$ and simultaneously the temperature reaches 2000K, molecular hydrogen begins to dissociate. Owing to effective cooling by dissociation, the first core begins collapse dynamically. Using a typical accretion rate of $10^{-5}M_\odot/\text{yr}$, the timescale in the first-core phase is only 5×10^3 yr, which is one or two orders of magnitude shorter than the Class 0 phase. This means that the expected number of the first-core objects is only a few hundredth of Class 0 objects. Besides, the fact that first-core objects are deeply embedded in their parental molecular cores prevents detection.

Such difficulties are being overcome with a rapidly in-

creasing number of observed young stellar objects, as well as with dramatical improvement of the sensitivity in the infrared/submillimeter wavelengths. Encouraged by these facts, the search for protostars in their earliest phase is being undertaken vigorously. Among them, Onishi, Mizuno, & Fukui (1999) found L1527F (also known as MC27) in Taurus by the H^{13}CO^+ emission, which is a candidate for an object in the earliest stage of a protostar owing to its very high density ($\sim 10^6\text{cm}^{-3}$). Recently, a central submillimeter source (L1521F-IRS) and near-mid infrared bipolar reflection nebulae with a luminosity $0.05L_\odot$ was detected in this object by *Spitzer Space Telescope* (Bourke et al. 2006). Another more promising object is Cha-MMS1, whose evolutionary stage appears to lie between L1527F and a starless core L1544 from the degree of N_2H^+ fractionation and from the detection of a mid-infrared source that is several times less luminous than L1521F-IRS (Belloch et al. 2006).

Knowledge of expected observational appearance of first-core objects is crucial in finding such objects and confirming their identity. Some efforts have already been made along this line. Boss & Yorke (1995) presented the expected spectral energy distribution of an object in the first-core phase, using the result of a three dimensional simulation of star formation. By performing a one-dimensional radiative hydrodynamical calculation, Masunaga, Miyama & Inutsuka (1998) followed the formation and evolution of the first cores, and presented the evolution of their emission spectrum. The above mentioned hydrodynamical studies, however, failed to follow the structure of the postshock flow of the accretion shock due to its extreme thinness, although the majority of emission is created there (Stahler, Shu, & Taam 1980). In ad-

dition to this, those authors included only the dust thermal emission in their calculation. In this paper, we take another approach. With a simpler assumption concerning the dynamics of the accreting envelope, we correctly solve the structure and emission process in the postshock flow. Using the injection radiation from the shock, we solve radiative transfer in the protostellar envelope. In this way, we obtain the observable radiation spectrum from the first-core object.

The organization of this paper is as follows. In Section 2, we describe the model for calculating the emission from the first-core objects. In Section 3, we present the results. In Section 4, we summarize this paper, and present a discussion and the conclusion.

2. Model

In Figure 1, we present a schematic view of our model of a first core and its envelope. For the structure and evolution of the envelope, we adopt a self-similar solution. Given the radius of the first core, which is the location of the accretion shock, the shock velocity and preshock density are obtained from a self-similar solution. Chemical and radiative processes in the postshock relaxation layer are analyzed by assuming a steady state shock. Finally, using the radiative energy injection obtained as mentioned above, we solve the radiative transfer in the envelope. We describe specific procedures in the following.

2.1. Envelope density distribution

We adopt a similarity solution as an envelope density structure. Two types of similarity solutions, (i) the Larson-Penston (LP; Larson 1969; Penston 1969) and (ii) Shu (Shu 1977) solutions, are studied. In translating the similarity solutions to physical quantities, we assume isothermal evolution at 10K. In Figure 2, we show the density distributions in the envelope both for LP and Shu similarity solutions. The structure at three epochs, where the mass of the first core $M_{\text{FC}} = 0.0125, 0.025$ and $0.05 M_{\odot}$, is illustrated for each model. As the maximum mass of the first core, we take $M_{\text{FC,max}} = 0.05 M_{\odot}$ following Masunaga & Inutsuka (2000). As the total mass of the core, i.e. the sum of the first-core mass and the envelope mass, we take $1 M_{\odot}$. In both solutions, the density low follows $\rho \propto r^{-3/2}$ for inner radius and becomes steeper, $\propto r^{-2}$, outside. The rarefaction wave, which separates the inner and outer parts, propagates outward at the sound speed. In the outer region, the Shu solution coincides with the singular isothermal sphere, while the density of the LP solution is 4.4 times higher.

Note that even with the same M_{FC} , the time which elapsed since the formation of the first core is different for the two solutions. Since the mass-accretion rate is $\dot{M} = 46.9 c_s^3 / G = 7.5 \times 10^{-5} M_{\odot} / \text{yr}$ ($\dot{M} = 0.975 c_s^3 / G = 1.6 \times 10^{-6} M_{\odot} / \text{yr}$) for the LP (Shu, respectively) solution, which is constant for isothermal similarity solutions, the age of the first core is $t_{\text{FC}} = M_{\text{FC}} / \dot{M}$, and its entire lifetime is $t_{\text{FC,max}} = M_{\text{FC,max}} / \dot{M} = 670 \text{yr}$ for the LP solution, and $3.2 \times 10^4 \text{yr}$ for the Shu solution. For the same

first-core mass, the rarefaction wave propagates to about a 50-times larger radius in the Shu solution than in the LP one. Thus, the LP solution is hardly modified, except at the innermost region, while the Shu solution evolves remarkably during the first-core stage (see Figure 2).

We take the radius of the first core, R_{sh} , as a free parameter. For the fiducial case, we take $R_{\text{sh}} = 5 \text{AU}$ from the spherical symmetric model (Masunaga, Miyama, & Inutsuka 1998). We fix the radius in time because it is found to be almost constant from hydrodynamical simulations (Masunaga et al. 1998). Taking account of the possibility that rotating first cores can be more flattened and extended (Saigo & Tomisaka 2006), we also study the case of $R_{\text{sh}} = 10 \text{AU}$ in order to mimic this effect. We then consider four models that are combinations of either LP or Shu solutions, and either $R_{\text{sh}} = 5$, or 10AU . These four models are called as LP05, LP10, S05, and S10, hereafter. At a given time, the mass inside R_{sh} is used as the first core mass, M_{FC} .

2.2. Structure and radiative processes in the postshock relaxation layer

The postshock flow is treated as a steady-state shock problem. The preshock density is given by a self-similar solution once the shock radius is fixed. The preshock temperature is given by solving radiative transfer in the envelope (Sec. 2.3).

Using the shock velocity v_s , Mach number \mathcal{M} , preshock pressure p_1 and number density n_1 , the postshock initial values can be obtained by the following Rankin-Hugoniot relations:

$$\frac{p_2}{p_1} = \frac{2\gamma_{\text{ad}}\mathcal{M}^2 - (\gamma_{\text{ad}} - 1)}{\gamma_{\text{ad}} + 1}, \quad (1)$$

$$\frac{v_2}{v_s} = \frac{n_1}{n_2} = \frac{(\gamma_{\text{ad}} - 1) + 2/\mathcal{M}^2}{\gamma_{\text{ad}} + 1}, \quad (2)$$

where we use subscript 1 (2) for the preshock (postshock, respectively) variables, and γ_{ad} is the ratio of specific heat.

In the postshock relaxation layer, since the gas kinetic temperature T is higher than the radiation temperature T_{rad} , the thermal energy is converted to the radiation energy. We follow the evolution of a postshock gas parcel until T reaches $1.1T_{\text{rad}}$ in the following way. The equations of conservation of mass and momentum fluxes,

$$\rho v = \rho_2 v_2 \equiv j, \quad (3)$$

$$\rho v^2 + p = \rho_2 v_2^2 + p_2, \quad (4)$$

can be incorporated in a single equation,

$$p + \frac{j^2}{\rho} = \rho_2 v_2^2 + p_2 = \text{const.} \quad (5)$$

Coupling the above relation with the equation of state for an ideal gas

$$p = \frac{\rho k_B T}{\mu m_H}, \quad (6)$$

we solve the energy equation

$$\frac{de}{dt} = -p \frac{d}{dt} \left(\frac{1}{\rho} \right) - \frac{1}{\rho} \Lambda, \quad (7)$$

where the energy density per unit mass is

$$e = \frac{k_B T}{(\gamma_{\text{ad}} - 1) \mu m_H}, \quad (8)$$

and Λ is the radiative cooling rate. This determines the structure of the postshock flow.

The radiative cooling is by line emission and dust thermal emission,

$$\Lambda = \Lambda_{\text{line}} + \Lambda_{\text{gr}}. \quad (9)$$

In the first term Λ_{line} , we include the fine-structure and metastable transitions of C, C⁺ and O, and molecular rotational transitions of H₂, CO, OH and H₂O. Those are treated as in Omukai et al. (2005), but the related coefficients for CO and H₂O are updated using those in Leiden Atomic and Molecular Database (Schöier et al. 2005). The cooling rate per unit volume by a transition i is

$$\Lambda_i = h\nu_i n(i_u) A_i \beta_i, \quad (10)$$

where $n(i_u)$ is the population in the upper level i_u , and A_i is the spontaneous radiative decay rate. The effect of photon-trapping is accounted for by the escape probability (Neufeld & Kaufman 1993), which is given by using the optical depth at the line centroid τ_i

$$\beta_i = \frac{1}{1 + 3\tau_i}, \quad (11)$$

and

$$\tau_i(s) = \int \alpha_i(s') ds', \quad (12)$$

where s is the distance from the shock. The above integral is over flows with $|v(s') - v(s)| < [\Delta v_D(s') + \Delta v_D(s)]/2$, where Δv_D is the thermal Doppler width. The second term in equation (9) is the cooling rate by the dust continuum

$$\Lambda_{\text{gr}} = 4\pi \int \kappa_\nu [B_\nu(T_{\text{dust}}) - B_\nu(T_{\text{rad}})] d\nu, \quad (13)$$

where κ_ν is the dust opacity and T_{dust} is the dust temperature. The dust opacity is taken from the IPS (“iron-poor” silicate) composite aggregates model of Semenov et al. (2003), who extended Pollack et al. (1994)’s calculation. The dust temperature is calculated by the energy balance between radiative loss from the dust and collisional heating by gas (see Omukai et al. 2005 for details). The postshock flow is optically thin to the dust continuum. Among radiative cooling processes mentioned above, the H₂O emission and dust thermal emission are dominant.

Chemical processes among compounds of H, C and O are included, as in Omukai (2000), where the reaction rate coefficients for the C and O chemistry are based on Millar et al. (1997). Hydrogen is assumed to initially be fully molecular. The initial abundances of other species in the gas phase are set to be $y(\text{CO}) = 1.10 \times 10^{-4}$, $y(\text{C}) = 1 \times 10^{-6}$, $y(\text{O}) = 3.31 \times 10^{-4}$, and $y(\text{H}_2\text{O}) = 1.7 \times 10^{-5}$ following Pollack et al. (1994)’s “Cloud Cores” model in their Table 1D. If the postshock temperature is higher than

the evaporation temperature of ice, which is about 150K, molecules locked in the ice are released into the gas phase. In this case, the amounts of H₂O, CO and CO₂ in the ice mantle $y_{\text{ice}}(\text{H}_2\text{O}) = 9.3 \times 10^{-5}$, $y_{\text{ice}}(\text{CO}) = 2.8 \times 10^{-5}$, and $y_{\text{ice}}(\text{CO}_2) = 5.9 \times 10^{-5}$ are added to the gas-phase chemistry.

2.3. Radiative Transfer in the Envelope

To solve the temperature structure in the envelope and the final processed radiation, we need to specify the injection radiation from the accretion shock, which is the sum of the emission from the postshock relaxation layer and radiation from interior of the first core. In the previous section, we described the method to calculate the emission from the relaxation layer. At the bottom of this layer, the radiation and matter are thermally well-coupled. Thus the radiation intensity is given by the blackbody radiation at temperature $T_{\text{rad}} = T_{\text{post}}$, where T_{post} is the temperature there. To find the post relaxation temperature T_{post} , we follow Stahler, Shu, & Taam (1981). For the LP solution, the envelope is optically thick both to the shock emission and to dust re-emission in the envelope. In this case, both the preshock temperature T_{pre} and the temperature at the bottom of the postshock relaxation layer T_{post} are equal to the radiation temperature in the postshock layer, which is optically thin. Thus, the condition

$$T_{\text{post}} = T_{\text{pre}} \quad (14)$$

needs to be satisfied. For the Shu solution, the envelope is optically thick to high energy shock emission, but optically thin to dust re-emission. In this case, the condition for T_{post} becomes

$$T_{\text{post}} = \left[\frac{1}{\sigma} \left(\frac{3}{4} F_{\text{pre}} - \frac{1}{4} F_{\text{post}} \right) \right]^{1/4}, \quad (15)$$

where F_{pre} (F_{post}) is the radiation energy flux in the preshock flow (at the bottom of the relaxation layer, respectively).

Using the postshock relaxation temperature T_{post} obtained above, the injection radiation to the envelope from the accretion shock is

$$I_{\nu, \text{in}} = I_{\nu, \text{shock}} + I_{\nu, \text{core}} = \frac{1}{2} \dot{E}_{\nu, \text{sh}} / \pi + B_\nu(T_{\text{post}}), \quad (16)$$

where $\dot{E}_{\nu, \text{sh}}$ is the energy emission rate in the postshock layer per unit area, and can be obtained by integrating the radiative cooling rate along the postshock flow,

$$\dot{E}_{\nu, \text{sh}} = \int \Lambda_\nu ds = \int \Lambda_\nu v dt, \quad (17)$$

where Λ_ν is the radiative cooling rate per unit frequency. The factor 1/2 in the first term on the right hand side of equation (16) comes from the fact that the other half of the radiation goes into the first core.

The radiation field in the envelope is determined by solving the radiative transfer under the input radiation from the inner boundary. We used the variable Eddington factor method (Mihalas & Mihalas 1984). The temperature T is determined by the radiative equilibrium

$$\int \kappa_\nu B_\nu(T) d\nu = \int \kappa_\nu J_{\nu, \text{dust}} + \sum_l \kappa_{\nu_l} J_l, \quad (18)$$

where $J_{\nu, \text{dust}}$ is the monochromatic mean intensity in the continuum, and J_l is the mean intensity integrated over frequency in a line l . Since the gas and dust are thermally coupled in the envelope, we do not distinguish their temperatures. In solving radiative transfer, we only consider the dust continuum as a source of opacity in the envelope. In all calculated mass ranges in the LP05 model and some in the LP10 model, the dust ice mantle sublimates and H_2O vapor exists in the innermost portion of the core. However, this part is also optically very thick to dust continuum, and the H_2O -line luminosity is significantly attenuated by the dust absorption in the surrounding region. Since we are not interested in such weak line emission, we do not include the H_2O -line opacity in our model.

2.4. Method of Model Construction

The model is constructed as follows:

- (i) Given the model parameters, namely, the shock radius R_{sh} and the type of similarity solution (LP or Shu).
- (ii) Calculate the shock velocity v_s and the preshock density ρ_1 for a given R_{sh} (§2.1). Then, assume the preshock temperature T_{pre} and the radiation temperature in the postshock layer T_{rad} .
- (iii) Solve the postshock flow (§2.2) and obtain the injection radiation field $I_{\nu, \text{in}}$ from the shock.
- (iv) Solve radiative transfer in the envelope (§2.3) and obtain T_{pre} .
- (v) If the assumed and calculated T_{pre} coincide and the shock boundary condition (eq. 14 or 15) is satisfied, the model is constructed. If not, go back to (ii) with modified T_{pre} and T_{rad} , and repeat this procedure until convergence.

3. Results

3.1. Emission in the postshock relaxation layer

In Figure 3, we present the temperature distribution in the postshock relaxation layer for three epochs with the first core mass being 0.0125, 0.025, and 0.05 M_\odot (i.e., 0.25, 0.5, and 1.0 $M_{\text{FC}, \text{max}}$, respectively). The distribution is shown as a function of the column density from the accretion shock: a higher column density corresponds to more downstream. The cooling rate by each cooling agent, namely, the dust thermal emission and the H_2O and H_2^{18}O line emission, is shown individually in Figure 4 for the same flows.

As can be seen in Figure 3, the postshock temperature T_2 is more dependent on the assumed first-core radius R_{sh} , rather than the type of similarity solution. It is 700–900K for the cases of $R_{\text{sh}} = 5$ AU, while $T_2 \simeq 400\text{K}$ for those of $R_{\text{sh}} = 10$ AU. This can be understood as follows. By assuming $\rho_1 v_s^2 \gg p_1$ in the preshock and $\rho_2 v_2^2 \ll p_2$ in the postshock,

$$\frac{1}{2} v_s^2 \simeq \frac{\gamma_{\text{ad}}}{\gamma_{\text{ad}} - 1} \frac{p_2}{\rho_2} = \frac{\gamma_{\text{ad}}}{\gamma_{\text{ad}} - 1} \frac{k_B T_2}{\mu m_{\text{H}}}. \quad (19)$$

Since the flow velocity is approximately given by free-fall

$$\frac{1}{2} v_s^2 \simeq \frac{GM_{\text{FC}}}{R_{\text{sh}}}, \quad (20)$$

the postshock temperature can be written as

$$T_2 \simeq \frac{\gamma_{\text{ad}} - 1}{\gamma_{\text{ad}}} \frac{\mu m}{k_B} \frac{GM_{\text{FC}}}{R_{\text{sh}}} \simeq 600\text{K} \left(\frac{M_{\text{FC}}}{0.05 M_\odot} \right) \left(\frac{R_{\text{sh}}}{5 \text{AU}} \right)^{-1}. \quad (21)$$

Since the equation above does not contain the type of similarity solution, the values of postshock temperature are similar for the two solutions with the same R_{FC} and M_{FC} . On the other hand, the dust temperature, which is close to the radiation temperature, is higher for the LP solutions, because of higher luminosity and higher optical depth in the envelope. Assuming the radiative diffusion equation

$$\frac{\partial T}{\partial r} = - \frac{3}{16\pi ac} \frac{\kappa_{\text{R}} \rho L}{r^2 T^3} \quad (22)$$

in the envelope and approximating the left hand side by T_1/R_{env} , where R_{env} is the outer radius of the envelope, we obtain

$$T_1^4 \propto \frac{\tau_{\text{env}} L}{R_{\text{sh}}^2}, \quad (23)$$

where τ_{env} is the envelope optical depth. This shows that the higher luminosity and higher envelope optical depth result in a higher radiation temperature ($\simeq T_1$) at the first-core surface.

Despite the smaller cooling rates (see Fig. 4), the shocked gas cools at a lower column density in the Shu models ($\lesssim 10^{20} \text{cm}^{-2}$) than in the LP ones ($\gtrsim 10^{20} \text{cm}^{-2}$). This is because of the longer timescale in the Shu cases: since the accretion rates of the LP and Shu solutions are different by a factor of about fifty, for the same column density the time which elapsed after the shock is also different by the same factor.

In all models, for low column densities, thermal energy in the postshock flow is dissipated mostly in dust continuum emission (see Fig.4). The postshock temperature is several hundred degree K (Fig.3), and increases with the first-core mass, reaching 900K (LP05) for $M_{\text{FC}, \text{max}} = 0.05 M_\odot$. In this temperature range, the most efficient molecular coolant is H_2O , and its cooling rate is as large as that by dust continuum for small column densities (see Fig.4). However, for $N_{\text{H}} \gtrsim 10^{19} \text{cm}^{-2}$, the H_2O lines become optically thick and the cooling rate decreases. The optical depth effect is apparent when we compare the H_2O cooling rate with that by its isotope H_2^{18}O , which remains optically thin.

In Figure 5, we show the contribution to the luminosity emitted in the postshock layer by the individual components; dust continuum, H_2O lines, H_2^{18}O lines, and OH lines. Although the contribution of the H_2O -line cooling to the shock dissipation increases with the first-core mass, the maximum fraction of radiated energy in the H_2O lines is at most about 10%, except for the S05 model. In S05 model, the H_2O -line cooling is as important as the dust continuum at the end of the first-core phase

$M_{\text{FC}} = 0.05M_{\odot}$. In this model, since the postshock gas temperature is high (700K) and it takes a long time for the layer to become optically thick, the H_2O lines contribute to cooling as much as the dust emission.

The contribution of the water isotope H_2^{18}O is very small owing to its small abundance. The second important species as a coolant is OH. However, its role is only temporary: since OH is intermediate species in chemical reactions leading to H_2O formation, its cooling rate decreases as OH is being converted to H_2O .

The value of the H_2O luminosity is dependent on the H_2O fraction as well as the gas temperature. In Figure 6, we show the H_2O and O concentrations at the bottom of the postshock relaxation layer. In LP05 model, the postshock dust temperature is higher than the evaporation temperature of the ice, even in our minimum mass case of $0.0125M_{\odot}$. Thus a large amount of water vapor [$y(\text{H}_2\text{O}) = 1.1 \times 10^{-4}$] is already present just below the shock. For the lowest mass case $M_{\text{FC}} = 0.0125M_{\odot}$, the final H_2O concentration remains almost the same as the initial value (Fig. 6 a). In the cases with higher mass, the final H_2O concentration increases with M_{FC} by a chemical process in the postshock flow owing to higher temperature and thus higher H_2O production rate (Wagner & Graff 1987; Kaufman & Neufeld 1996). For $M_{\text{FC}} \gtrsim 0.025M_{\odot}$, most of the remaining oxygen, which is not locked to CO, is converted to H_2O via OH. This can be observed as a decrease in the OH luminosity (Fig. 5 a). In the LP10 model, the ice mantle evaporates for $M_{\text{FC}} > 0.028M_{\odot}$. This can be seen as the discontinuous rise in the H_2O concentration, as well as the H_2O luminosity (Fig. 5 b). Additional H_2O production by chemical reactions slightly increases the H_2O concentration in the high- M_{FC} cases. The ice mantles do not evaporate in either the S05 or S10 model. In the S05 model, additional H_2O is produced by high-temperature gas-phase chemistry for $M_{\text{FC}} \gtrsim 0.03M_{\odot}$, while in the S10 model H_2O hardly increases from the initial value of $y(\text{H}_2\text{O}) = 1.7 \times 10^{-5}$.

In Table 1, we list the important transitions, their energy fluxes $F_{\text{line,sh}} = \frac{1}{2}\dot{E}_{\text{line,sh}}$ and the luminosities

$$L_{\text{line}} = 4\pi R_{\text{sh}}^2 F_{\text{line,sh}}, \quad (24)$$

generated in the postshock relaxation layer. The emitted luminosities are higher and the wavelengths of the strongest emission lines are shorter for LP / small R_{sh} cases than for the Shu / large R_{sh} cases. In general, the emitted radiation from the shock is subject to absorption and re-emission in the envelope (Sec. 3.2), and thus these values does not correspond to the observable line luminosities. However, if cavities are present in the envelope due to outflow, rotation, etc., the shock emission can come out unattenuated. In this case, the emission lines listed in Table 1 are observable probably as mid-infrared nebula.

3.2. Processed Radiation through the Envelope

A first-core object is enshrouded with an optically thick envelope, where radiation emitted from the accretion shock is absorbed and reemitted as dust thermal

radiation. The total optical depths of the envelopes for each frequency are shown for the LP05 and S05 models in Figure 7. The envelope is optically thick at wavelengths shorter than 1mm in the LP05 model (LP10: $600\mu\text{m}$, S05: $100\mu\text{m}$, S10: $75\mu\text{m}$, respectively). With increasing mass of the first core, the inner portion of the envelope is accreted and the optical depth decreases. This is not a large effect compared with the differences between the LP and Shu models.

Figure 8 shows the temperature distribution in the envelope. For the LP models, the dust photosphere locates at ~ 30 AU, outside of which the envelope is optically thin and reemitted photons escape freely. The temperature falls approximately as $T \propto r^{-1}$ and $T \propto r^{-1/3}$ in optically thick and thin regimes, respectively (e.g., Sec. 4.2 of Hartmann 1998). Below its vaporization temperature ($\simeq 150$ K), H_2O ice is an important contributor to the opacity. Therefore, for $\gtrsim 150\text{K}$, due to evaporation of ice mantle of dust, the dust opacity is reduced. This causes the flattening of temperature profile in the innermost region observed in the LP models. For the Shu models, where the envelope is optically thin, the temperature obeys $T \propto r^{-1/3}$ in the entire envelope.

Figure 9 shows the spectrum of processed dust radiation, i.e. the radiation escaping from the envelope. The emitted dust radiation $L_{\nu} = 4\pi R_{\text{sh}}^2 \dot{E}_{\nu,\text{sh}}$ in the shock is also shown for comparison. However, the peak of the shock emission locates at rather short wavelength, around $10\text{--}100\mu\text{m}$, due to high temperature in the postshock flow, while that of processed radiation appears at longer wavelength, $100\mu\text{m}\text{--}1\text{mm}$, which reflects the lower envelope temperature.

The envelopes of the LP models are optically thick both to the shock and the processed radiation, while those of the Shu models are optically thick to the emitted radiation, but optically thin to the re-emission. Owing to this difference, the processed spectra of the LP models resemble the blackbody radiation $L_{\nu} \propto B_{\nu} \propto \nu^2$ on the Rayleigh-Jeans side, while those of the Shu model have flatter spectra in low frequencies $L_{\nu} \propto \nu^{1/2}$ approximately (Fig. 9). This flat spectrum is explained by the following consideration. The radiation spectrum from optically thin medium is

$$L_{\nu} = 4\pi \int \kappa_{\nu} B_{\nu} dM \propto \nu^{3+\beta-(3-n)/m} \simeq \nu^{1/2}, \quad (25)$$

for density and temperature distributions $\rho \propto r^{-n}$ and $T \propto r^{-m}$, and an opacity of $\kappa_{\nu} \propto \nu^{\beta}$. In the above, we used $n = 3/2$, $m = 1/3$ and $\beta = 2$. Comparing the LP and Shu models with the same R_{sh} , we notice that, although the peak frequency of the shock emission is higher in the LP models, that of the processed radiation is lower owing to the larger optical depth of the envelope.

In Figures 11-14, we show the emitted and processed luminosities of the H_2O lines in three different epochs for all the models. For the emitted luminosities, i.e. the unattenuated luminosities before processing in the envelope (eq. 24), the corresponding values of energy flux at the shock $F_{\text{line,sh}}$ are also indicated on the left axis. We also

present in Table 2 the luminosities and the line flux at the distance of 150pc for the ten strongest H₂O emission lines at the epoch of $M_{\text{FC}} = 0.05M_{\odot}$. Among H₂O emission lines from the shock in the LP models (see Figures 11 and 12), those with frequencies $\sim 10^{13}\text{Hz}$ ($30\mu\text{m}$) have the highest luminosities $\sim 10^{-4} - 10^{-5}L_{\odot}$. These lines are, however, heavily attenuated in the envelope owing to the high optical depth in these frequencies. On the other hand, the peak in processed line radiation appears around 10^{12}Hz ($300\mu\text{m}$), where the optical depth of the envelope is about a few. With such small values of the processed luminosities $10^{-8} - 10^{-10}L_{\odot}$, those lines are completely buried in the dust continuum: $L_{\text{line}}/\Delta v_{\text{D}} \ll L_{\nu, \text{dust}}$, where Δv_{D} is the Doppler width of the line. In the Shu models, line emission in the shock peaks around 10^{13}Hz ($30\mu\text{m}$), which is similar to that in the LP model. The processed line emission, however, peaks around $3 \times 10^{12}\text{Hz}$ ($100\mu\text{m}$), higher than in the LP models owing to the smaller optical depth in the Shu models. With maximum luminosities of $10^{-6} - 10^{-7}L_{\odot}$, the monochromatic luminosities of these lines are higher than that of the dust continuum. The final processed luminosities in the dust continuum and the H₂O lines are shown in Figure 10. In the LP models, the H₂O luminosities are only $\sim 10^{-6}$ of the dust luminosities, while in the Shu models, about 1% of the radiation is still in H₂O lines after reprocessing in the envelope.

Profiles of brightness temperature are shown for different wavelength bands in Figures (15)-(18). These figures show that in low frequencies where the envelopes are optically thin, the emission from the first cores is directly visible. Then, a discontinuity appears in the brightness temperature distribution at the radius of the first core. On the other hand, at the shorter wavelengths, where the envelope is optically thick, only the emission from the dust photosphere in the envelope is visible. With increasing observing frequency, the brightness temperature at the center decreases and the discontinuity at the first-core surface disappears.

4. Summary and Discussion

We calculated the radiation spectrum of young stellar objects in their first-core phase. As envelope models, we studied cases of the Larson-Penston (LP) and the Shu self-similar solutions. In the LP model, the emitted spectrum has a peak at $\sim 10\mu\text{m}$ both for the dust continuum and H₂O lines. The optical depth of the envelope at this frequency is 100 – 1000, such that virtually all of the shock emission is absorbed in the envelope and reemitted as the dust thermal emission at lower frequencies. The amount of total luminosity remains unchanged, which is $0.01 - 0.1L_{\odot}$, but the emission peak is shifted to lower frequency owing to the lower temperature in the envelope. The processed spectrum can be approximated by the blackbody radiation with temperature 30K, which peaks at $200\mu\text{m}$. Our result for the continuum spectrum is consistent with a previous study by Masunaga & Inutsuka (2000). In the Shu models, the amount of total luminosity is $10^{-4} - 10^{-3}L_{\odot}$, which is smaller by almost two orders of

magnitude than in the LP model owing to the smaller accretion rate by a similar factor. The dust temperature in the postshock layer is lower ($\lesssim 100\text{K}$), and thus the wavelength of the emission peak is longer ($\sim 40\mu\text{m}$) than that in the LP case ($\sim 10\mu\text{m}$). However, owing to the lower optical depth in the envelope, the peak of the processed spectrum is at a shorter wavelength (100 – $200\mu\text{m}$) than that in the LP case.

Strong H₂O emission from accreting protostars has already been pointed out by Neufeld & Hollenbach (1994), who considered the shock on the surface of circumstellar disks of more evolved objects. They carried out a parameter study for shocks with a preshock density of $n_1 = 10^{7.5} - 10^{12}\text{cm}^{-3}$ and a velocity $v_s = 5 - 100\text{km/s}$, and calculated the emission from them. Although, in their calculations, protostars tend to be more massive, and shocks are thus stronger than ours ($n_1 = 10^9 - 2 \times 10^{11}\text{cm}^{-3}$ and $v_s = 1 - 4\text{km/s}$ in our models), our shock calculations and results are very similar to their weakest shock cases. Provided that shock conditions are similar, it is a difficult task to distinguish observationally whether the shock is on the disk surface or on the stellar surface without spatially resolving the emission region. In the case of accretion onto the disk, the amount of dust extinction can be smaller than that in our case. Using this fact, we might be able to tell the geometry of the shock. We need more studies in the future to confirm this possibility.

So far, we have discussed the case of spherical symmetry, where the envelope absorbs the shock emission and reemits it at the longer wavelengths. In practice, however, outflows are observed almost ubiquitously in very young stellar objects, such as Class 0 objects. Theoretically, it is known that outflows can be launched as early as the first-core phase (Machida et al. 2006). Even without outflow, a flattened disk-like density distribution is realized by the presence of angular momentum (Terebey, Shu, & Cassen 1984). Thus, it is highly plausible that the envelope is optically thin in the polar direction while it is optically thick in the equatorial (disk) one. If so, the shock emission escapes unattenuated and can be observed directly in the polar direction, or as a reflection nebula in other directions. In these cases, the radiation is mostly emitted in the mid-infrared range, and about 10% of the emission is in H₂O lines at similar wavelengths (see Table 1).

In this paper, we demonstrated that observations in mid- to far-infrared and submillimeter wavelengths are important for finding the first-core objects. Among observational facilities at these wavelengths, we examine observational feasibilities by currently operating *Spitzer Space Telescope* (*Spitzer*) and *Stratospheric Observatory for Infrared Astronomy* (*SOFIA*), as well as forthcoming *Herschel Space Observatory*, *Atacama Large Millimeter/submillimeter Array* (*ALMA*) and *SPace Infrared telescope for Cosmology and Astrophysics* (*SPICA*). *Spitzer* has a spectroscopic line sensitivity of $\sim 10^{-18}\text{W/m}^2$ in mid-infrared wavelengths ($\sim 30\mu\text{m}$) and a photometric sensitivity of $\sim 0.1\text{mJy}$ at $10\mu\text{m}$ and $\sim 10\text{mJy}$ at $100\mu\text{m}$. Here we suppose the observation time to be one hour. The airborne telescope *SOFIA* has a spectroscopic

line sensitivity of $\sim 10^{-17}\text{W/m}^2$ at mid to far-infrared wavelengths ($5 - 200\mu\text{m}$) and photometric sensitivity of $\sim 1\text{mJy}$ at $10\mu\text{m}$ and $\sim 30\text{mJy}$ at $100\mu\text{m}$. *Herschel* is a space telescope with its aperture 3.5m and observing wavelengths $60 - 700\mu\text{m}$. Its spectroscopic line sensitivity is $10^{-18} - 10^{-17}\text{W/m}^2$ in short wavelengths ($\lambda < 200\mu\text{m}$) and $10^{-17} - 10^{-16}\text{W/m}^2$ in longer wavelengths, while its photometric sensitivity is $1 - 10\text{mJy}$. The millimeter and submillimeter telescope *ALMA* observes at $300\mu\text{m} - 1\text{cm}$ (or $30 - 950\text{GHz}$), with its spectroscopic line sensitivity $\sim 10^{-20}\text{W/m}^2$ and photospheric sensitivity $\sim 0.1\text{mJy}$. Finally, *SPICA* is an infrared space telescope with a 3.5m aperture, the same as *Herschel*, but its mirror is cooled to 4.5K , far cooler than that of *Herschel* (80K). The observing wavelengths are from $5\mu\text{m}$ to 1mm , with its spectroscopic line sensitivity being $10^{-21} - 10^{-20}\text{W/m}^2$. Its photospheric sensitivity depends strongly on the wavelength: it is $\sim 1\mu\text{Jy}$ around $10\mu\text{m}$ and $\sim 1\text{mJy}$ around $100\mu\text{m}$.

Here, we evaluate the H_2O line flux from first-core objects. After attenuation in the envelope, the maximum value of the H_2O -line luminosities is $L_{\text{line}} \sim 10^{-7}L_{\odot}$ with its wavelength around $100\mu\text{m}$ in the Shu models, although it is significantly dimmer in the LP models. If there is a cavity in the envelope owing to outflow or rotation, and the shock radiation leaks through it without reprocessed in the envelope, the line luminosities take the maximum value at around $30\mu\text{m}$ both for the LP and Shu solutions, with its value being $L_{\text{line}} \sim 10^{-4}L_{\odot}$ (LP) or $L_{\text{line}} \sim 10^{-5}L_{\odot}$ (Shu), respectively (see Figures 11 - 14). Below, as a typical distance to a first-core object, we use 1kpc , farther than neighboring star-forming regions, because, for detection of such rare objects, the observation of a large number of young stellar objects is needed. The line flux can be given by

$$F_{\text{line}} = 3.4 \times 10^{-18}\text{W/m}^2 \left(\frac{L_{\text{line}}}{10^{-4}L_{\odot}} \right) \left(\frac{D}{1\text{kpc}} \right)^{-2} \quad (26)$$

$$= 3.4 \times 10^{-21}\text{W/m}^2 \left(\frac{L_{\text{line}}}{10^{-7}L_{\odot}} \right) \left(\frac{D}{1\text{kpc}} \right)^{-2}, \quad (27)$$

where we use typical values of the luminosities for unattenuated ($10^{-4}L_{\odot}$) and attenuated radiation ($10^{-7}L_{\odot}$) in the first and second expressions, respectively. If the shock emission from a first core is visible without attenuation in the envelope, *Spitzer* is able to detect it in sources as far as 1kpc . If sources are closer, *SOFIA* also has chance to observe them. However, their sensitivities at far-infrared wavelengths are not enough for observing the attenuated emission. On the other hand, *SPICA* can detect both processed line radiation through the envelope and direct radiation from the accretion shock as far as 1kpc . Owing to lack of the sensitivity at the mid-infrared wavelengths, the other future telescopes cannot observe shock radiation. As for the attenuated line radiation, which appears in the submillimeter range, the sensitivity of *Herschel* is not sufficient. Although sensitivity of *ALMA* appears to be sufficient, absorption by telluric water vapor prohibits the observation of H_2O lines in the submillimeter range.

Next we discuss the observability of the dust contin-

uum. Using a typical value $\nu L_{\nu} = 10^{-3}L_{\odot}$ at a typical wavelength of processed radiation $\lambda = 200\mu\text{m}$ (see Figure 9), the flux of dust continuum is

$$F_{\nu} = 2.4\text{mJy} \left(\frac{\nu L_{\nu}}{10^{-3}L_{\odot}} \right) \left(\frac{D}{1\text{kpc}} \right)^{-2}, \quad (28)$$

which falls below the sensitivities of currently operating *SOFIA* and *Spitzer*, but is above those of all three future telescopes discussed here. In particular, having sensitivity both for direct and processed radiation, *SPICA* is most suitable for observing the first-core objects not only by the H_2O emission, but also by the dust continuum.

In summary, *SPICA* can observe first-core objects as far as 1kpc by far-infrared dust emission and (if the collapse is Shu-like) by the H_2O emission. In addition, if the hot dust emission and H_2O high-excitation-line emission in the mid-infrared wavelengths originating from the accretion shock come out unattenuated through a possible cavity, *SPICA* can detect them as direct or reflection light, depending on the orientation between the cavity and the observer.

We thank Y. Fukui, S. Inutsuka, S. Narita, T. Onishi, K. Saigo, and Y. Yonekura for suggestions, and the anonymous referee for improving the manuscript. This study is supported in part by the Grants-in-Aid by the Ministry of Education, Science and Culture of Japan (16204012; 18740117; 18026008).

References

- Belloche, A., Parise, B., van der Tak, F. F. S., et al. 2006, A&A, 454, L51
- Bourke, T. L., Myers, P. C., Evans II, N. J., et al. 2006, ApJ, 649, L37
- Boss, A. P. & Yorke, H. W. 1995, ApJ, 439, L55
- Inutsuka, S. 2004, in "Star Formation: Theory and Modelling" Springer, Proceedings in Physics 91, "The Dense Interstellar Medium in Galaxies", Edited by S. Pfalzner, C. Kramer, C. Staubmeier, & A. Heithausen, p.575
- Hartmann, L. 1998, Accretion Processes in Star Formation (Cambridge Univ. Press)
- Hayashi, C. 1966, ARA&A, 4, 171
- Kaufman, M. J., & Neufeld, D. A., 1996, ApJ, 456, 611
- Larson, R. B. 1969, MNRAS, 145, 271
- Lee, J.-E., Bergin, E. A., & Evans, N. J., II 2004, ApJ, 617, 360
- Machida, M. N., Inutsuka, S. & Matsumoto, T. 2006, ApJL, in press, astro-ph/0603456
- Masunaga, H., & Inutsuka, S. 2000, ApJ, 531, 365
- Masunaga, H., Miyama, S. M., & Inutsuka, S. 1998, ApJ, 495, 346
- Mihalas, D., & Mihalas, B. W. 1984, Foundations of Radiation Hydrodynamics (Oxford Univ. Press)
- Neufeld, D. A., & Kaufman, M. J. 1993, ApJ, 418, 263
- Neufeld, D. A. & Hollenbach, D. J. 1994, ApJ, 428, 170
- Omukai, K. 2000, ApJ, 534, 809
- Omukai, K., Tsuribe, T., Schneider, R., & Ferrara, A. 2005, ApJ, 626, 627
- Onishi, T., Mizuno, A., & Fukui, Y. 1999, PASJ, 51, 257
- Penston, M. V. 1969, MNRAS, 144, 425
- Pollack, J. B, Hollenback, D., Beckwith, S., Simonelli, D. P., Roush, T., & Fong, W. 1994, ApJ, 421, 615
- Saigo, K. & Tomisaka, K. 2006, ApJ, 645, 381
- Semenov, D., Henning, Th., Helling, Ch., Ilgner, M., & Sedlmayr, E. 2003, A&A, 410, 611
- Schöier, F. L., van der Tak, F. F. S., van Dishoeck E. F., Black, J. H. 2005, A&A432, 369
- Shu, F. H. 1977, ApJ, 214, 488
- Shu, F. H., Adams, F. C., & Lizano, S. 1987, ARA&A, 25, 23
- Terebey, S., Shu, F. H., & Cassen, P. M. 1984, ApJ, 286, 529
- Wagner, A. F. & Graff, M. M. 1987, ApJ, 317, 423
- Young, C. H. & Evans, N. J., II 2005, ApJ, 627, 293

model	transition	λ (μm)	L_{line} (L_{\odot})	$F_{\text{line,sh}}$ ($\text{erg s}^{-1} \text{ cm}^{-2}$)	model	transition	λ (μm)	L_{line} (L_{\odot})	$F_{\text{line,sh}}$ ($\text{erg s}^{-1} \text{ cm}^{-2}$)
LP05	$9_{27} - 8_{18}$	21.9	1.1E-4	6.2	LP10	$8_{36} - 7_{07}$	23.8	6.8E-5	9.2E-1
	$7_{70} - 6_{61}$	28.6	1.1E-4	6.1		$6_{61} - 5_{50}$	33.0	6.3E-5	8.5E-1
	$8_{45} - 7_{16}$	23.9	1.1E-4	6.0		$8_{45} - 7_{16}$	23.9	6.1E-5	8.4E-1
	$9_{36} - 8_{27}$	25.2	1.1E-4	5.7		$7_{25} - 6_{16}$	29.9	5.9E-5	8.1E-1
	$8_{36} - 7_{07}$	23.8	1.0E-4	5.6		$6_{34} - 5_{05}$	30.9	5.8E-5	8.0E-1
	$8_{54} - 7_{25}$	21.2	9.8E-5	5.3		$6_{52} - 5_{41}$	36.0	5.7E-5	7.8E-1
	$9_{45} - 8_{36}$	28.3	9.8E-5	5.3		$9_{27} - 8_{18}$	21.9	5.6E-5	7.6E-1
	$7_{61} - 6_{52}$	30.6	9.7E-5	5.3		$7_{52} - 6_{43}$	33.0	5.5E-5	7.5E-1
	$8_{54} - 7_{43}$	30.9	9.0E-5	4.9		$5_{50} - 4_{41}$	39.4	5.5E-5	7.5E-1
S05	$6_{61} - 5_{50}$	33.0	8.9E-5	4.9	S10	$7_{61} - 6_{52}$	30.6	5.4E-5	7.3E-1
	$6_{34} - 5_{05}$	30.9	1.2E-5	6.5E-1		$5_{23} - 4_{14}$	45.2	3.0E-6	4.1E-2
	$7_{25} - 6_{16}$	29.9	1.1E-5	6.1E-1		$3_{30} - 2_{21}$	66.5	2.9E-6	4.0E-2
	$5_{50} - 4_{41}$	39.4	1.1E-5	5.9E-1		$4_{32} - 3_{21}$	58.8	2.6E-6	3.5E-2
	$5_{41} - 4_{32}$	43.9	9.6E-6	5.2E-1		$4_{32} - 3_{03}$	40.7	2.5E-6	3.4E-2
	$8_{36} - 7_{07}$	23.8	9.6E-6	5.2E-1		$3_{21} - 2_{12}$	75.5	2.5E-6	3.4E-2
	$7_{34} - 6_{25}$	34.6	9.3E-6	5.1E-1		$4_{41} - 3_{30}$	49.4	2.5E-6	3.4E-2
	$6_{52} - 5_{41}$	36.0	9.2E-6	5.0E-1		$5_{32} - 4_{23}$	48.0	2.2E-6	3.0E-2
	$6_{43} - 5_{14}$	28.0	9.2E-6	5.0E-1		$4_{23} - 3_{12}$	78.8	2.1E-6	2.8E-2
	$4_{41} - 3_{30}$	49.4	8.8E-6	4.8E-1		$4_{22} - 3_{13}$	57.7	1.9E-6	2.6E-2
	$6_{61} - 5_{50}$	33.0	8.7E-6	4.7E-1		$6_{16} - 5_{05}$	82.1	1.8E-6	2.4E-2

Table 1. Most luminous H_2O lines emitted in the postshock layer before processing in the envelope at the epoch of $M_{\text{FC}} = 0.05M_{\odot}$

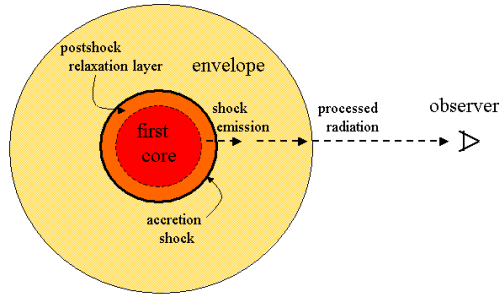


Fig. 1. First core and its environment (schematic). This shows our model geometry of the first core and the envelope. We calculated the processed radiation through the envelope, in addition to the emission from the accretion shock.

model	transition	λ (μm)	L_{line} (L_{\odot})	F_{line} at 150pc (W cm^{-2})	model	transition	λ (μm)	L_{line} (L_{\odot})	F_{line} at 150pc (W cm^{-2})
LP05	$3_{21} - 3_{12}$	258	7.5E-9	1.1E-20	LP10	$3_{21} - 3_{12}$	258	2.7E-8	4.1E-20
	$3_{12} - 3_{03}$	274	7.3E-9	1.1E-20		$3_{12} - 3_{03}$	274	2.7E-8	4.0E-20
	$4_{22} - 4_{13}$	249	5.7E-9	8.5E-21		$1_{11} - 0_{00}$	270	2.1E-8	3.1E-20
	$1_{11} - 0_{00}$	270	4.9E-9	7.4E-21		$4_{22} - 4_{13}$	249	2.0E-8	3.0E-20
	$2_{20} - 2_{11}$	244	4.6E-9	6.9E-21		$2_{20} - 2_{11}$	244	1.9E-8	2.9E-20
	$2_{11} - 2_{02}$	399	4.5E-9	6.8E-21		$3_{12} - 2_{21}$	260	1.7E-8	2.6E-20
	$5_{23} - 5_{14}$	213	4.4E-9	6.7E-21		$2_{02} - 1_{11}$	304	1.7E-8	2.5E-20
	$3_{12} - 2_{21}$	260	4.3E-9	6.4E-21		$3_{13} - 2_{02}$	139	1.7E-8	2.5E-20
	$2_{02} - 1_{11}$	304	4.1E-9	6.3E-21		$4_{13} - 3_{22}$	145	1.6E-8	2.3E-20
S05	$1_{10} - 1_{01}$	539	4.90E-9	5.9E-21	S10	$5_{23} - 5_{14}$	213	1.5E-8	2.3E-20
	$6_{16} - 5_{05}$	82.1	1.5E-6	2.2E-18		$3_{21} - 2_{12}$	75.5	1.1E-6	1.6E-18
	$5_{05} - 4_{14}$	99.6	1.3E-6	2.0E-18		$5_{05} - 4_{14}$	99.6	1.1E-6	1.6E-18
	$4_{23} - 3_{12}$	78.8	1.2E-6	1.9E-18		$4_{23} - 3_{12}$	78.8	1.0E-6	1.6E-18
	$4_{14} - 3_{03}$	114	1.1E-6	1.6E-18		$6_{16} - 5_{05}$	82.1	1.0E-6	1.5E-18
	$3_{21} - 2_{12}$	75.5	1.1E-6	1.6E-18		$4_{14} - 3_{03}$	114	1.0E-6	1.5E-18
	$6_{06} - 5_{15}$	83.4	1.1E-6	1.6E-18		$2_{21} - 1_{10}$	108	9.8E-7	1.5E-18
	$5_{15} - 4_{04}$	95.7	1.0E-6	1.6E-18		$3_{30} - 2_{21}$	66.5	8.4E-7	1.3E-18
	$2_{21} - 1_{10}$	108	1.0E-6	1.5E-18		$3_{22} - 2_{11}$	90.1	8.2E-7	1.2E-18
	$7_{07} - 6_{16}$	72.0	1.0E-6	1.5E-18		$2_{20} - 1_{11}$	101	7.8E-7	1.2E-18
	$3_{22} - 2_{11}$	90.1	1.0E-6	1.5E-18		$5_{15} - 4_{04}$	95.7	7.5E-7	1.1E-18

Table 2. Most luminous H_2O lines after processing in the envelope at the epoch of $M_{\text{FC}} = 0.05M_{\odot}$

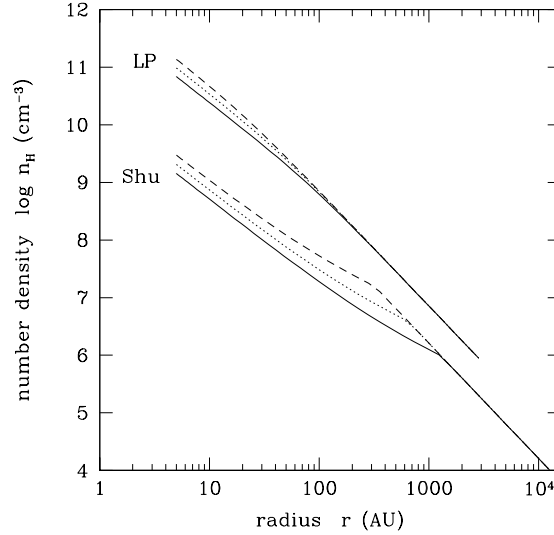


Fig. 2. Number density distributions in the envelope. Depicted are both of the LP and Shu solutions for three epochs of the first-core mass $M_{\text{FC}} = 0.0125M_{\odot}$ (dashed), $0.025M_{\odot}$ (dotted) and $0.05M_{\odot}$ (solid).

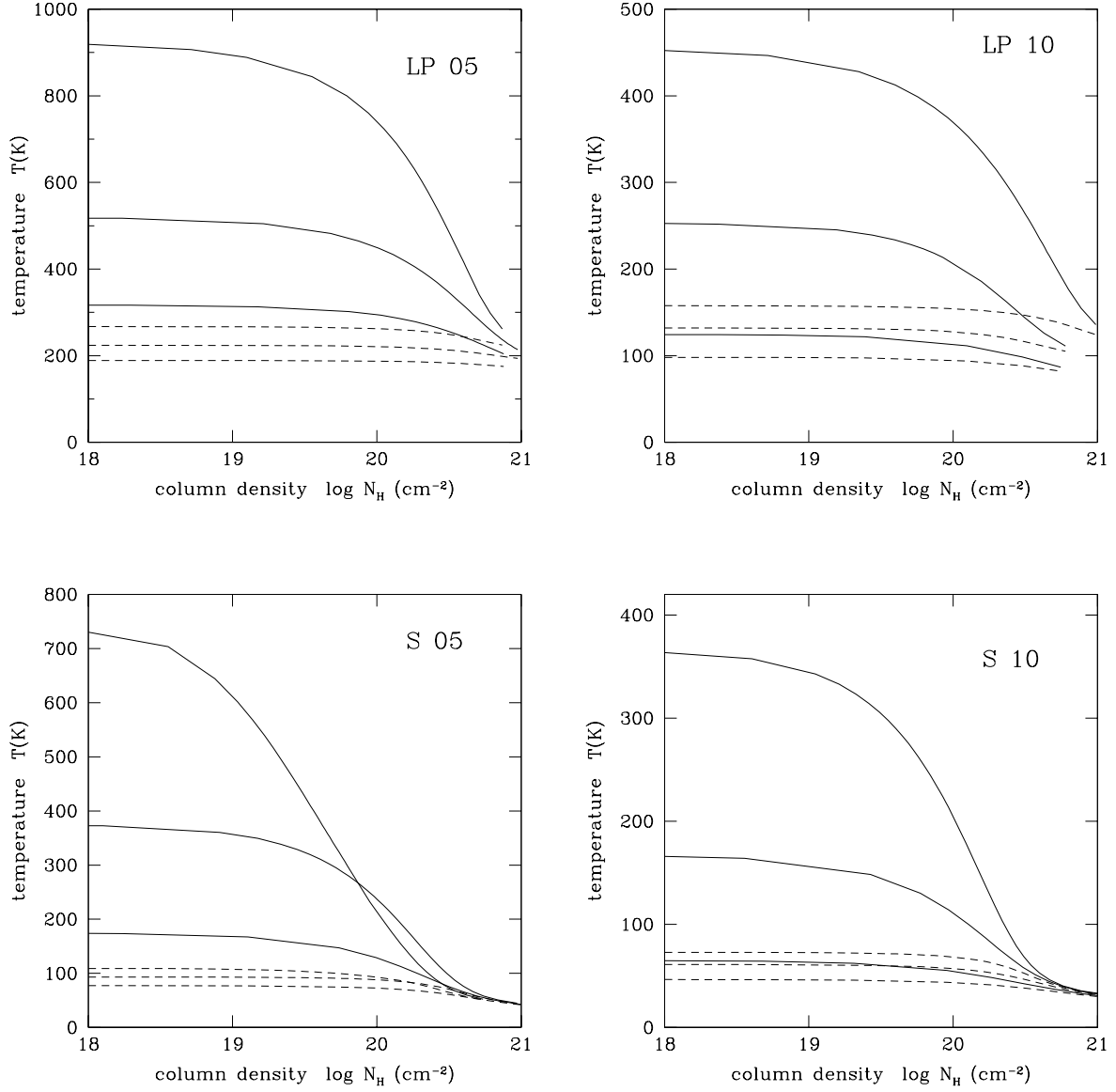


Fig. 3. Temperature distributions in the postshock relaxation layer. The panels are for (a) LP05, (b) LP10, (c) S05, (d) S10 models. For each model, those for three epochs of $M_{\text{FC}} = 0.0125M_{\odot}$ (bottom), $0.025M_{\odot}$ (middle) and $0.05M_{\odot}$ (top) are shown. The solid curves indicate the gas temperature, while the dashed ones are for the dust temperature.

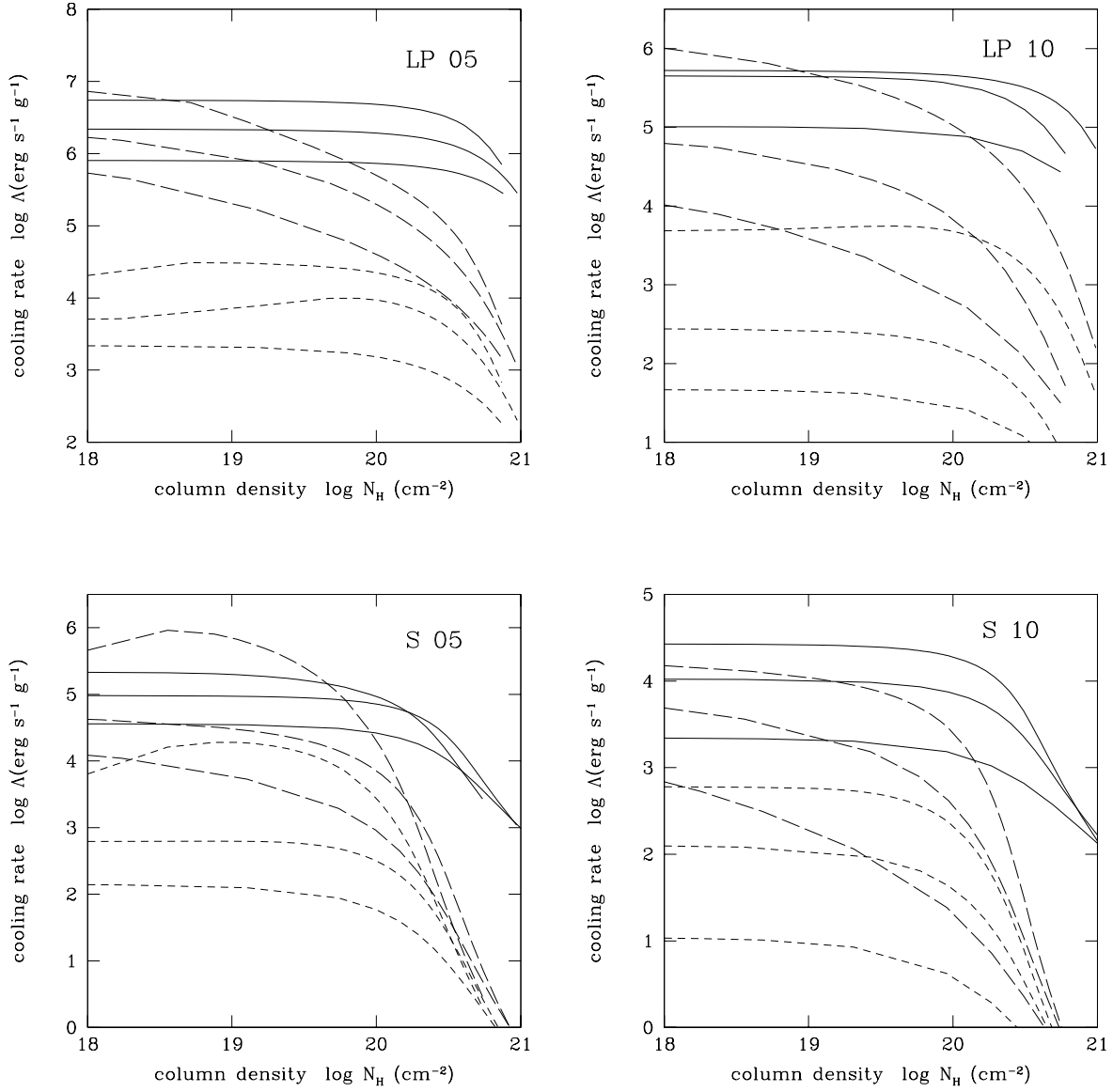


Fig. 4. Cooling rates in the postshock relaxation layer. The panels are for (a) LP05, (b) LP10, (c) S05, (d) S10 models. For each model, three epochs of $M_{\text{FC}} = 0.0125 M_{\odot}$ (bottom), $0.025 M_{\odot}$ (middle) and $0.05 M_{\odot}$ (top) are shown. The solid, dashed, and dotted curves indicate the cooling rates by dust, H_2O , and H_2^{18}O , respectively.

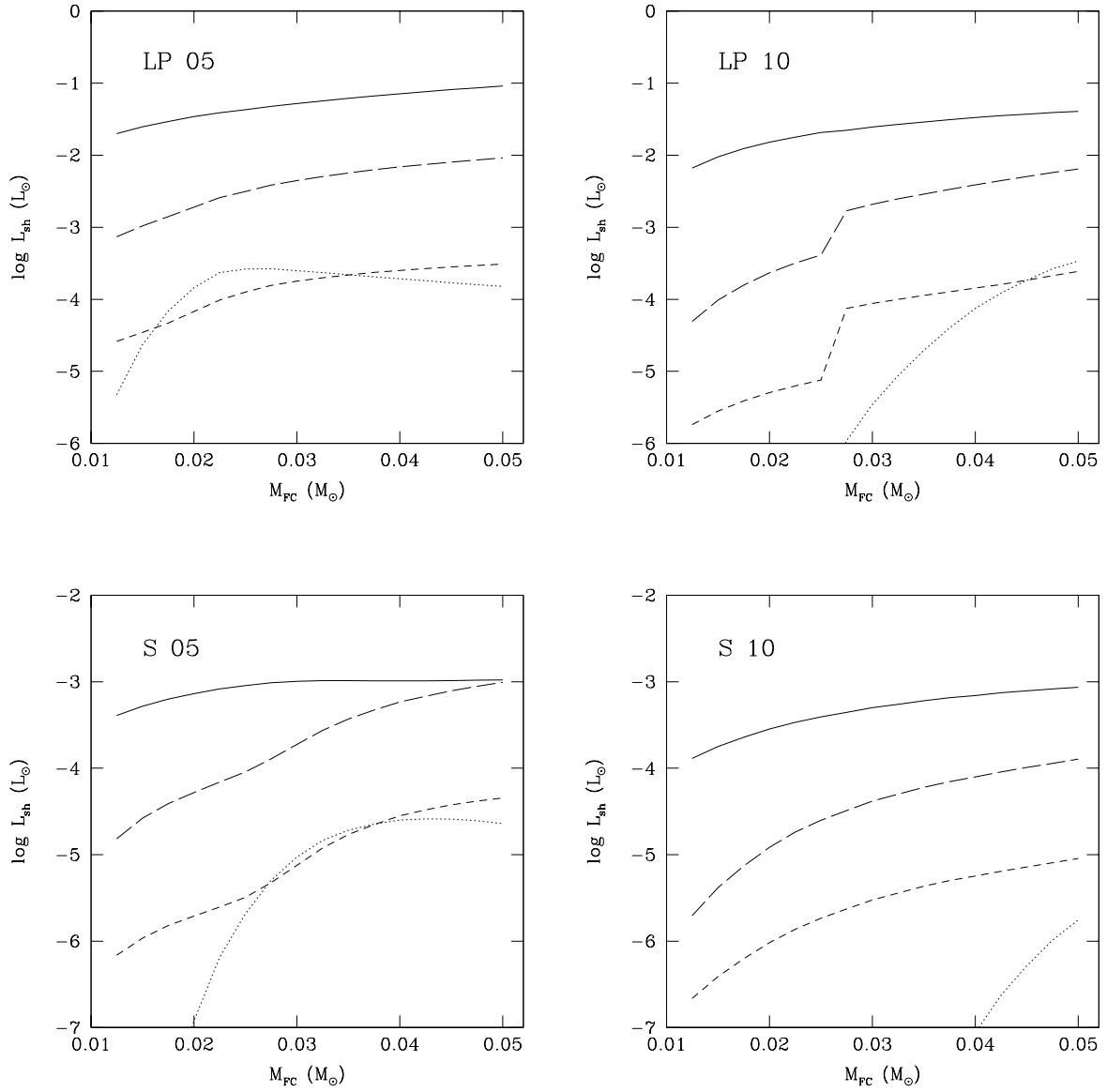


Fig. 5. Emitted luminosities in the postshock layer in the dust continuum (solid), H_2O lines (long-dashed), H_2^{18}O lines (short-dashed), and OH lines (dotted) as a function of the first-core mass. The panels are for (a) LP05, (b) LP10, (c) S05, (d) S10 models.

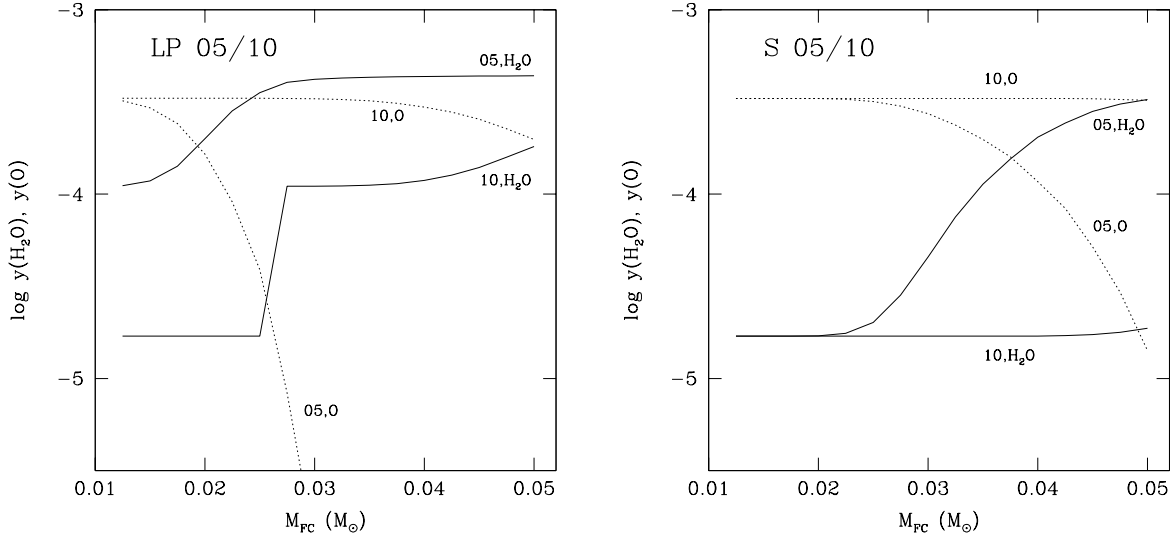


Fig. 6. H_2O (solid) and O (dashed) concentrations at the bottom of the postshock layer as a function of the first core mass. The panels are for (a) LP05 and 10, (b) S05 and 10 models.

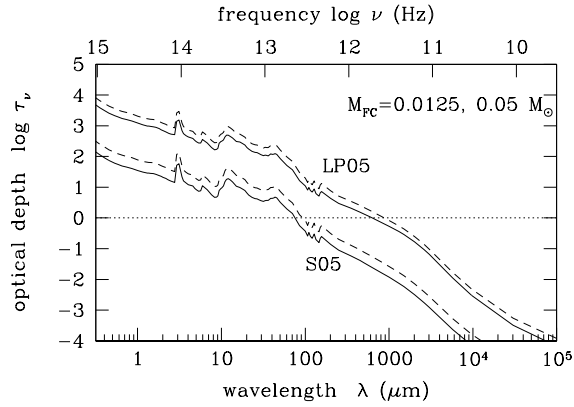


Fig. 7. Optical depth of the envelope for models LP05 and S05 as a function of the wavelength. The dashed and solid lines show the cases of $M_{\text{FC}} = 0.0125 M_{\odot}$ and $0.05 M_{\odot}$, respectively. The dotted horizontal line indicates where the optical depth is unity.

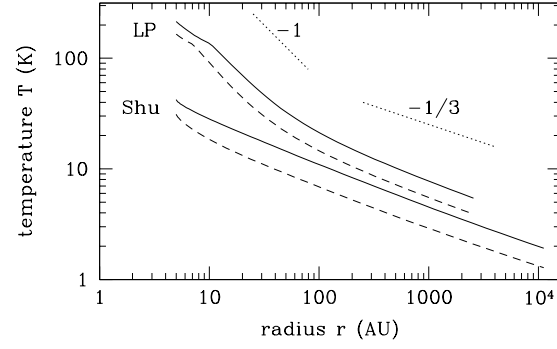


Fig. 8. Temperature distributions in the envelope. The dashed and solid lines show the distribution at epochs of $M_{\text{FC}} = 0.0125M_{\odot}$ and $0.05M_{\odot}$, respectively. Lines for $T \propto r^{-1/3}$ and $\propto r^{-1}$, which correspond to optically thick and thin cases, respectively, are also shown.

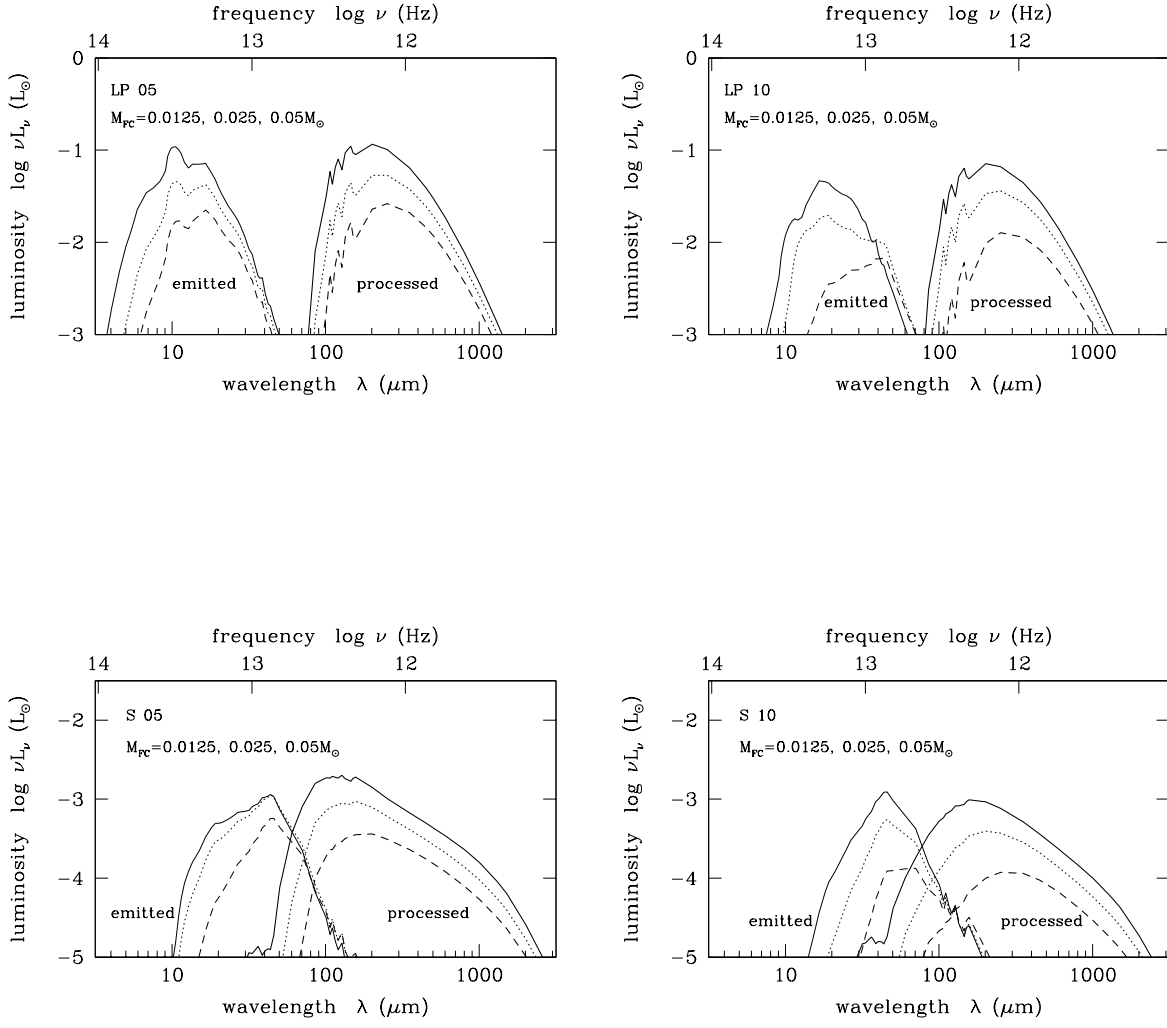


Fig. 9. Spectral energy distributions in the dust continuum of the first-core objects. Both the emitted (thin) and processed (thick) spectra are shown. The panels (a)-(d) show models LP05, LP10, S05, and S10, respectively. In each panel, the distributions are shown for three different epochs of $M_{\text{FC}} = 0.0125 M_{\odot}$ (dashed), $0.025 M_{\odot}$ (dotted), and $0.05 M_{\odot}$ (solid).

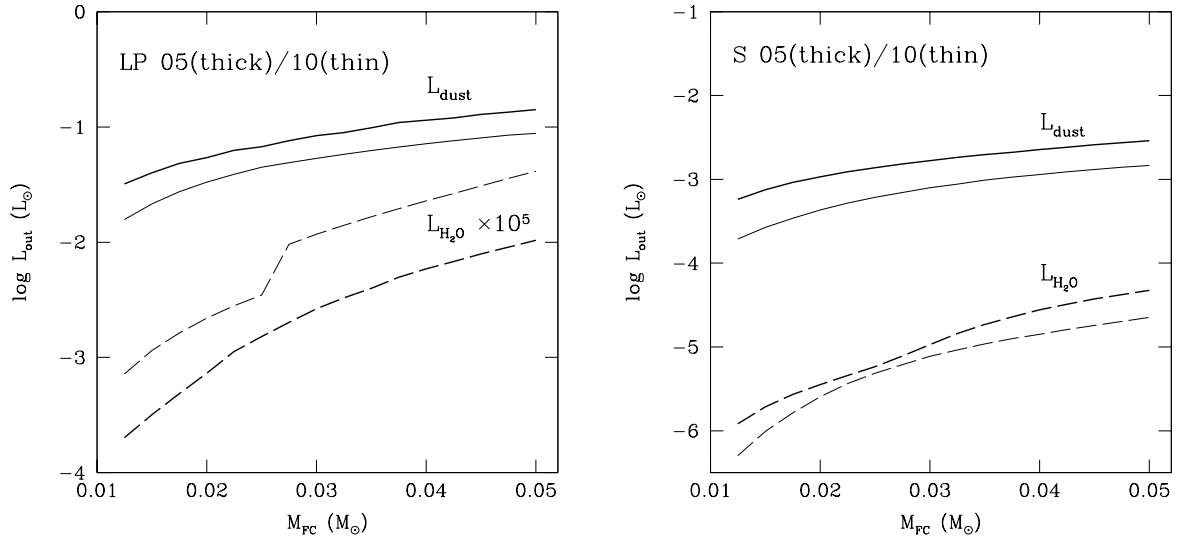


Fig. 10. Evolution of luminosities in the dust continuum (solid) and H₂O lines (dashed) at the outer boundary of the envelope, shown as a function of the first-core mass. The panels are for (a) LP05 (thick) and LP10 (thin) models, (b) S05 (thick) and S10 (thin) models. In panel (a), the luminosities in H₂O lines $L_{\text{H}_2\text{O}}$ is multiplied by 10^5 for clarity.

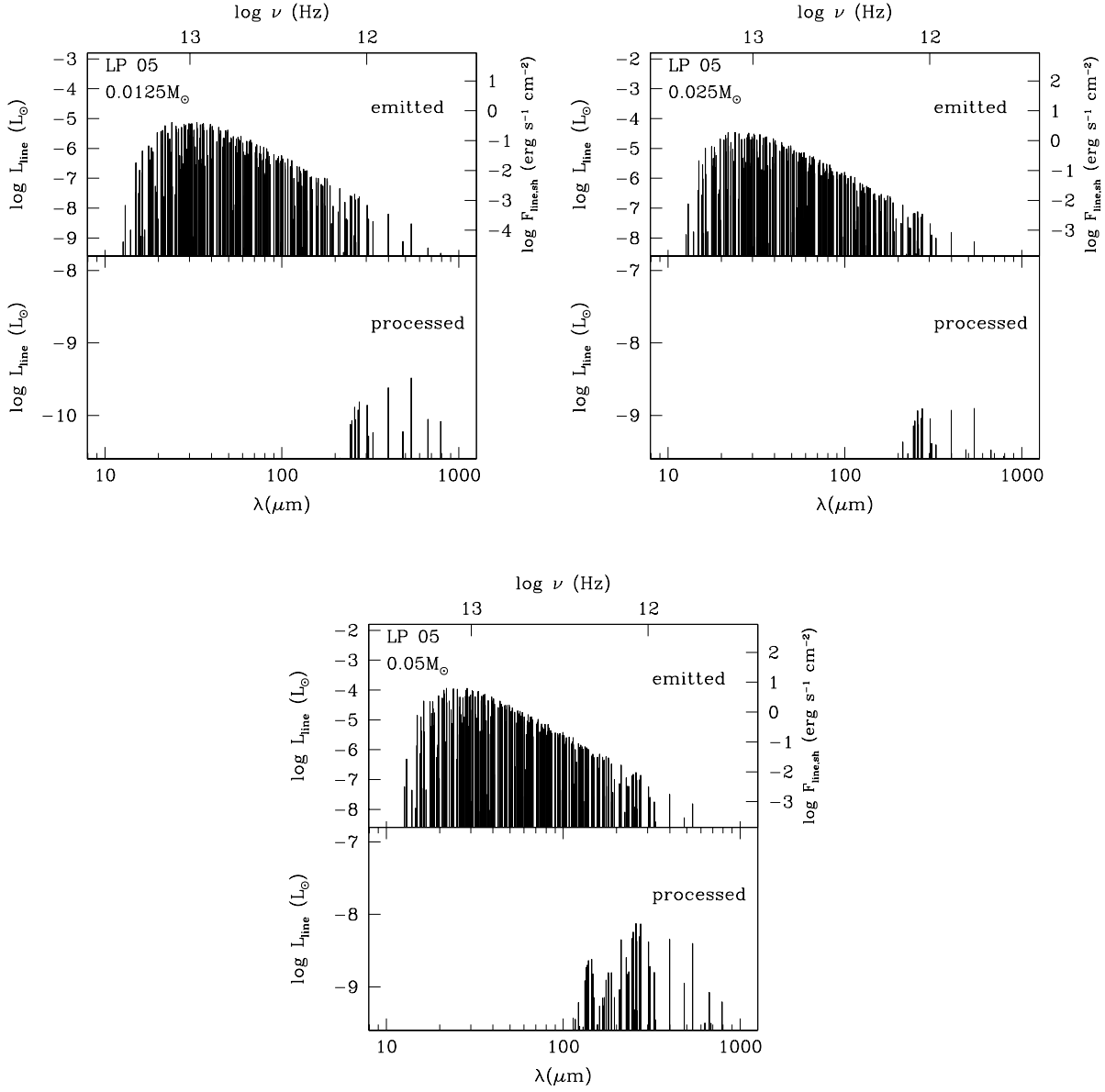


Fig. 11. Emitted (upper halves) and processed (lower halves) luminosities of H_2O lines for the LP05 model. Three epochs of (a) $0.0125M_\odot$ (b) $0.025M_\odot$ and (c) $0.05M_\odot$ are shown. In the upper halves, the values of the energy flux at the shock are also indicated.

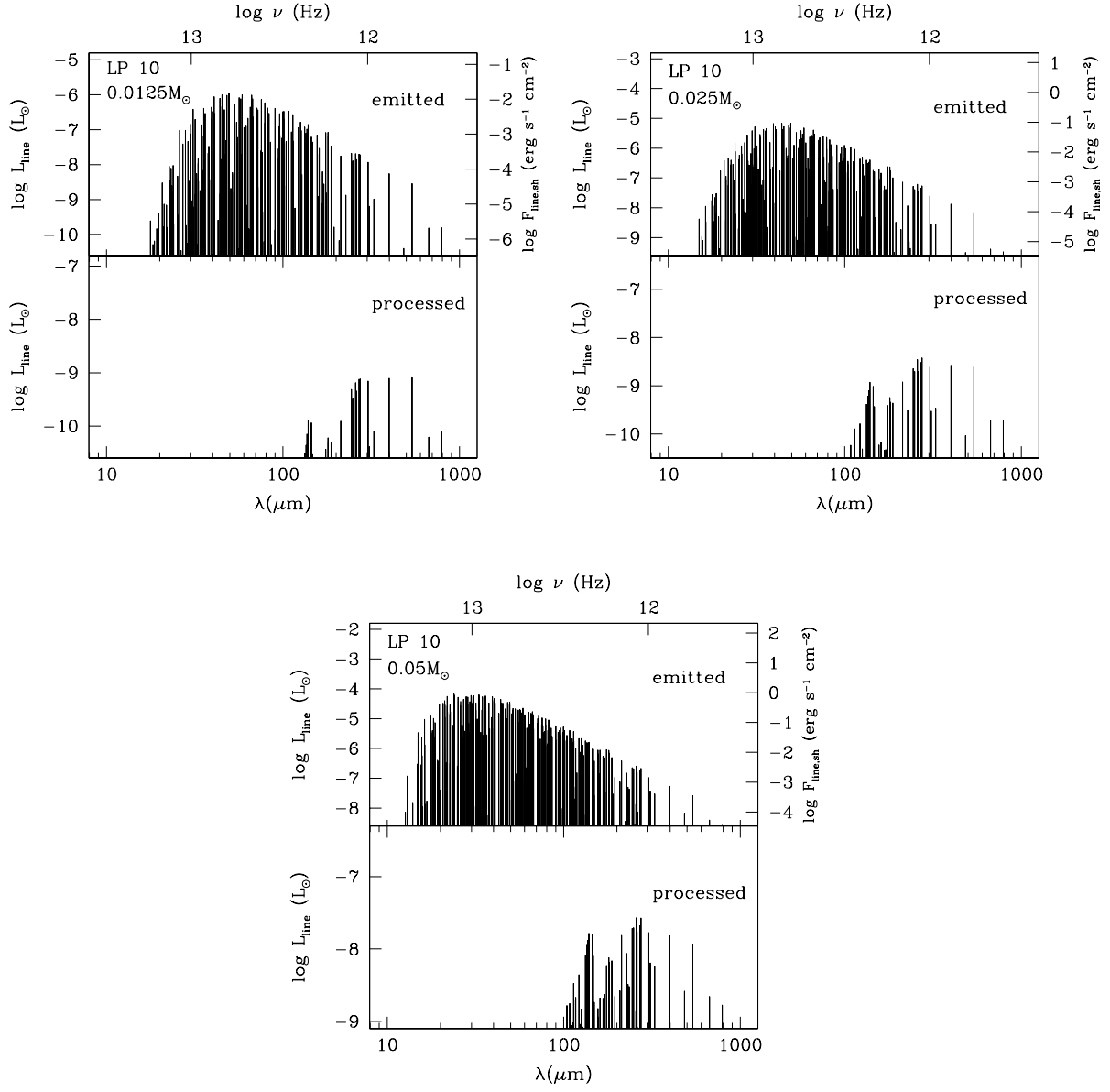


Fig. 12. Same as Figure 11, but for the LP10 model.

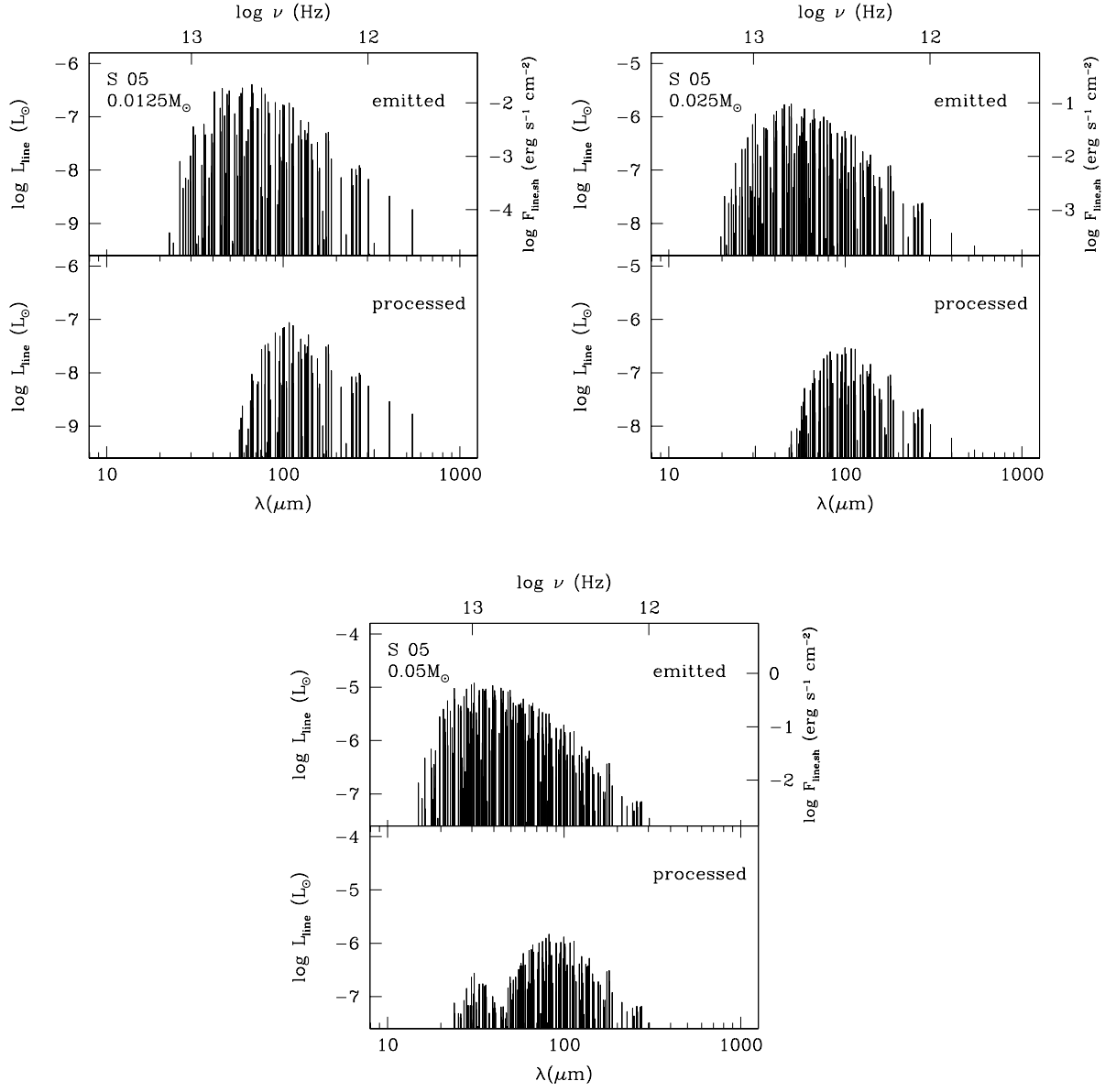


Fig. 13. Same as Figure 11, but for the S05 model.

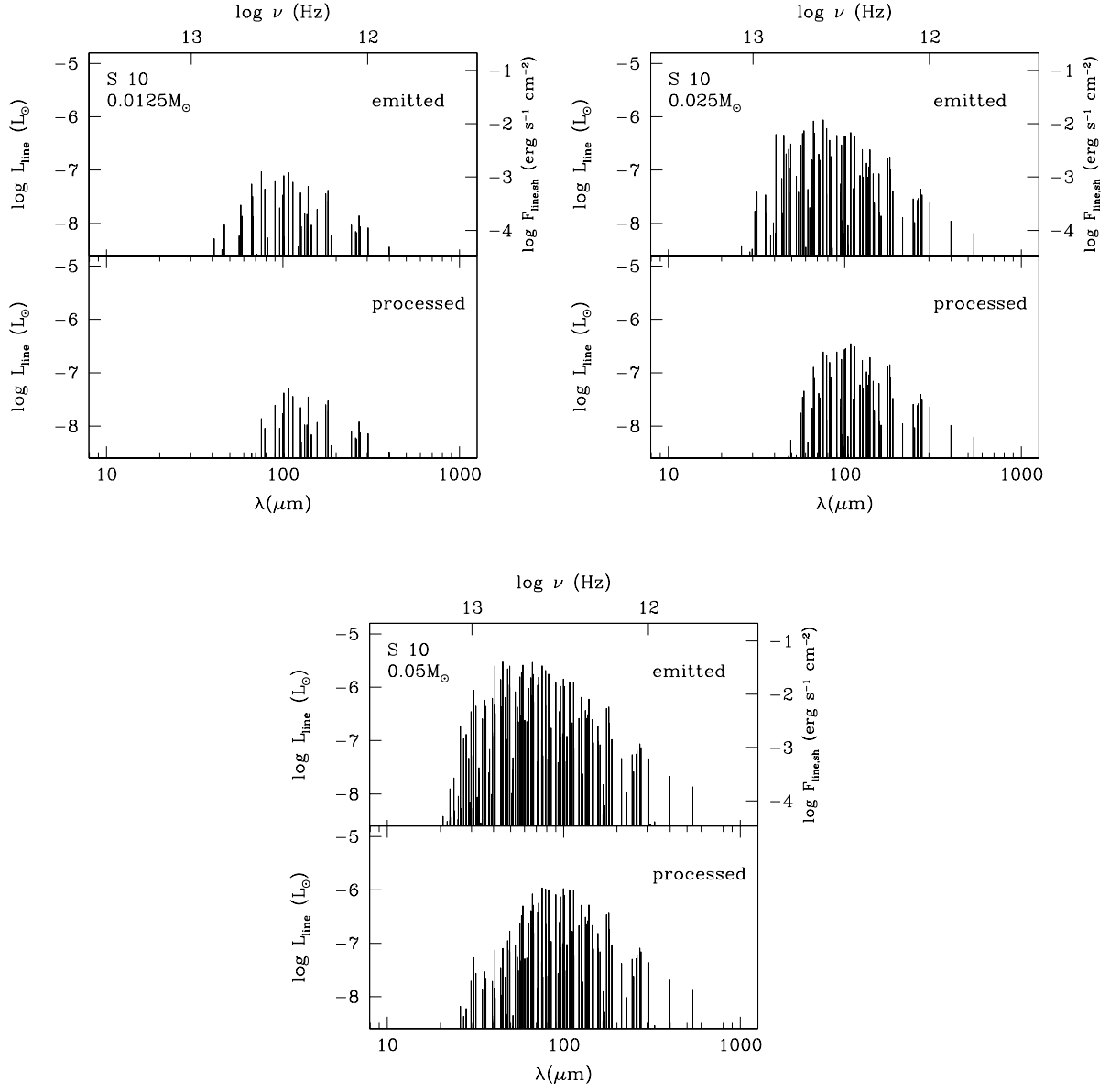


Fig. 14. Same as Figure 11, but for the S10 model.

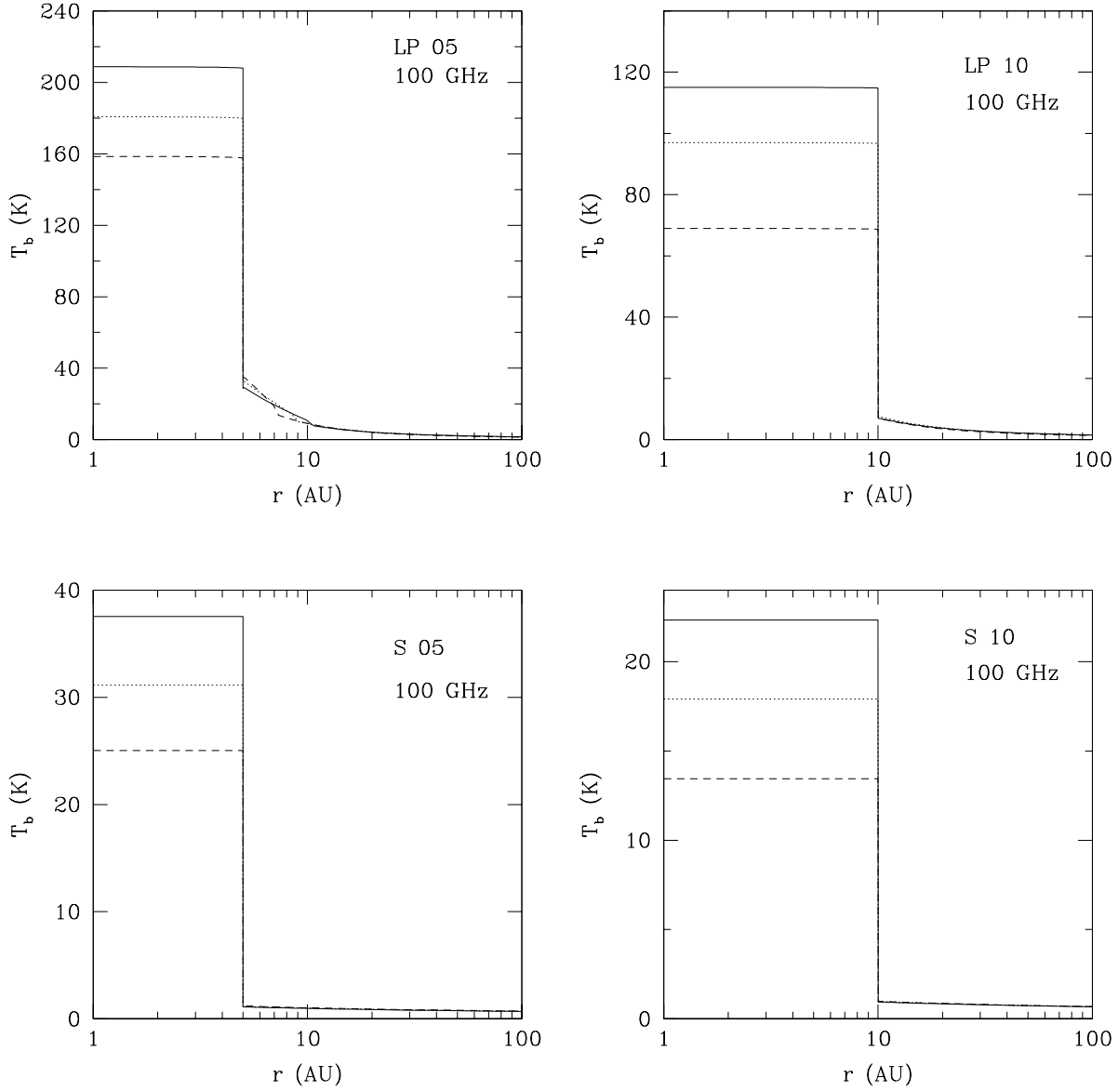


Fig. 15. Distribution of the brightness temperature at 100GHz as a function of the impact parameter of the line of sight. Panels (a)-(d) show LP05, LP10, S05, and S10 models, respectively. In each panel, the distributions are shown in three different epochs $M_{FC} = 0.0125 M_{\odot}$ (dashed), $0.025 M_{\odot}$ (dotted), and $0.05 M_{\odot}$ (solid).

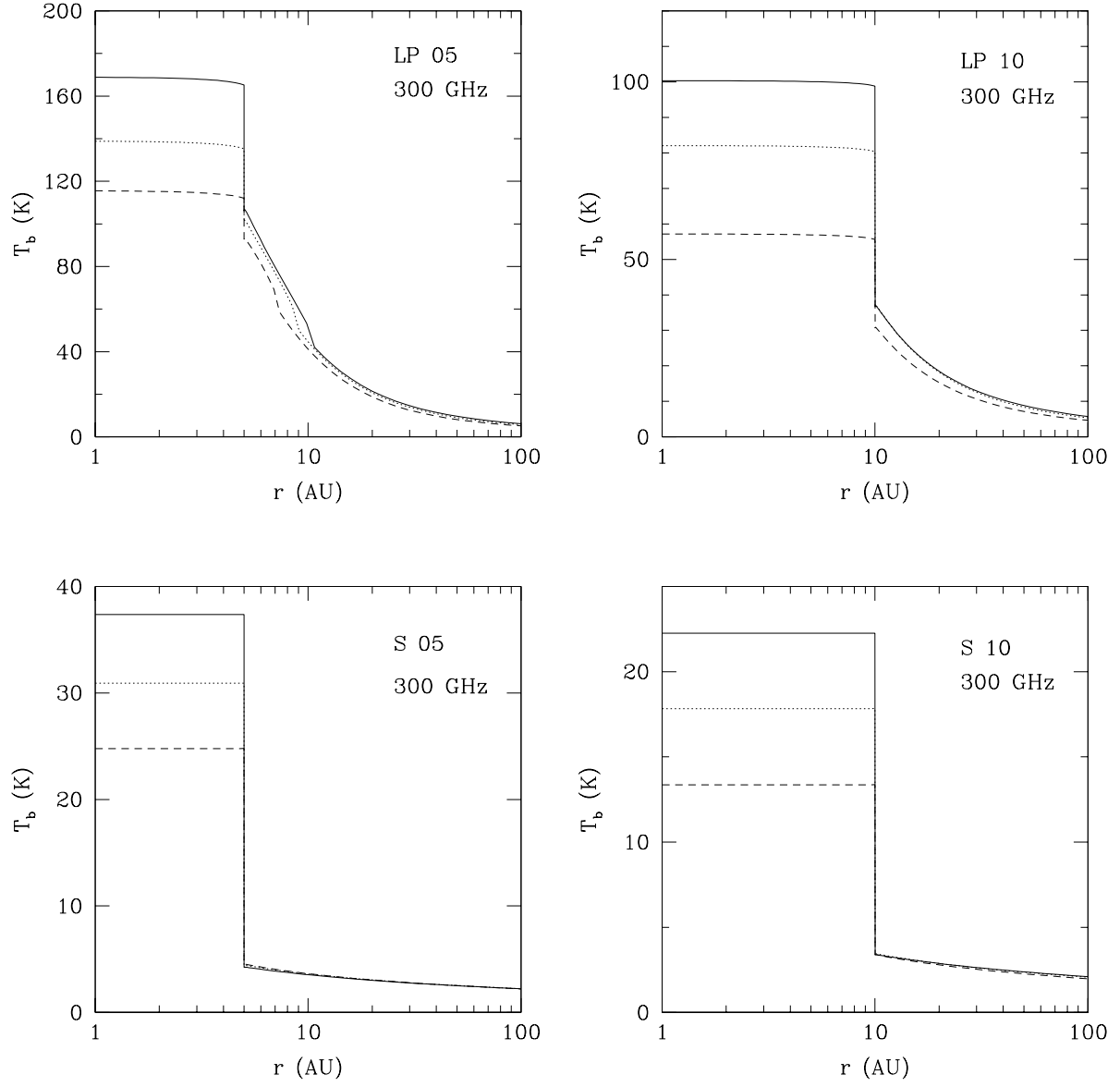


Fig. 16. The same as Figure 15 but for the observing frequency at 300GHz.

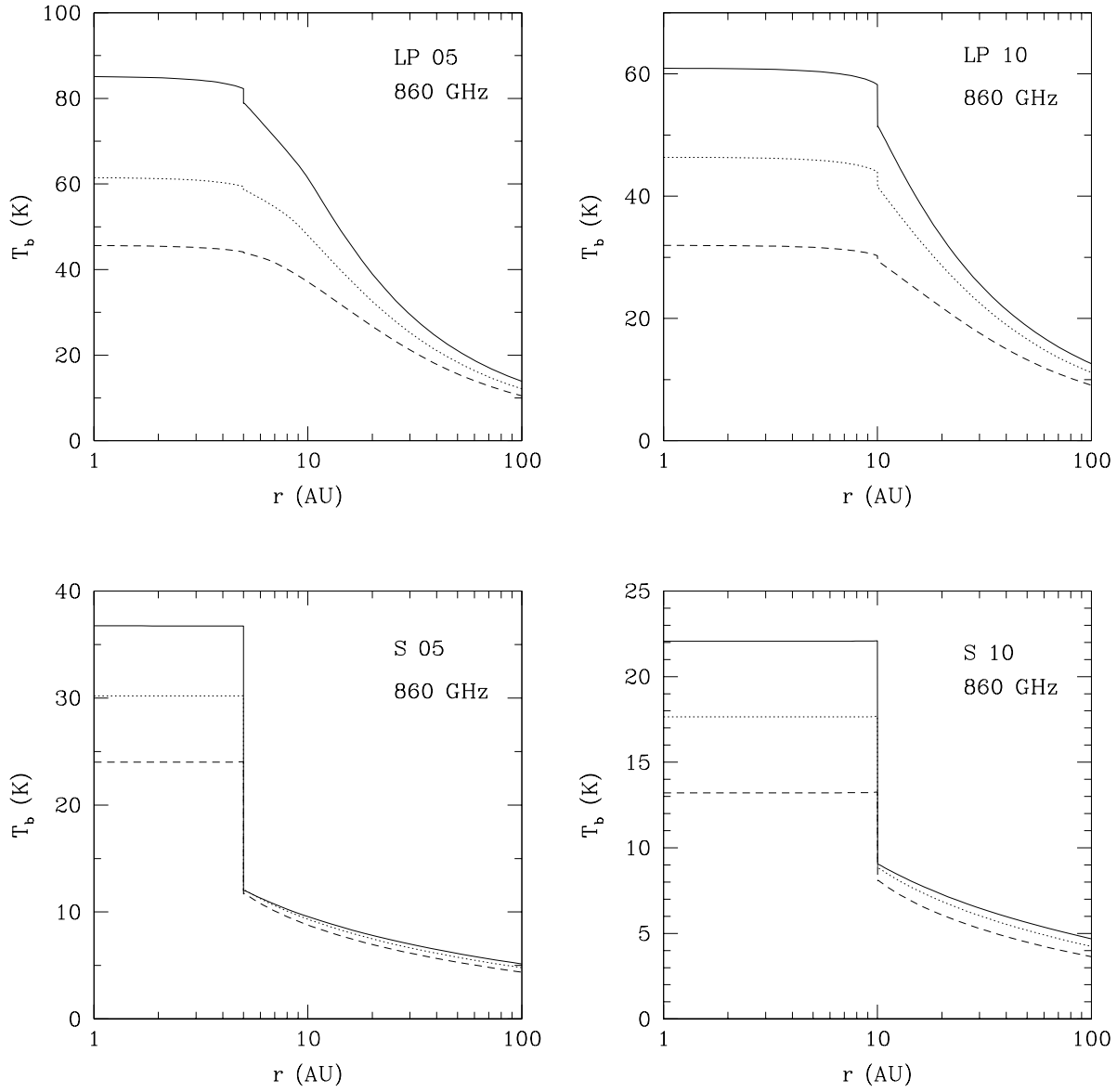


Fig. 17. The same as Figure 15 but for the observing frequency at 860GHz.

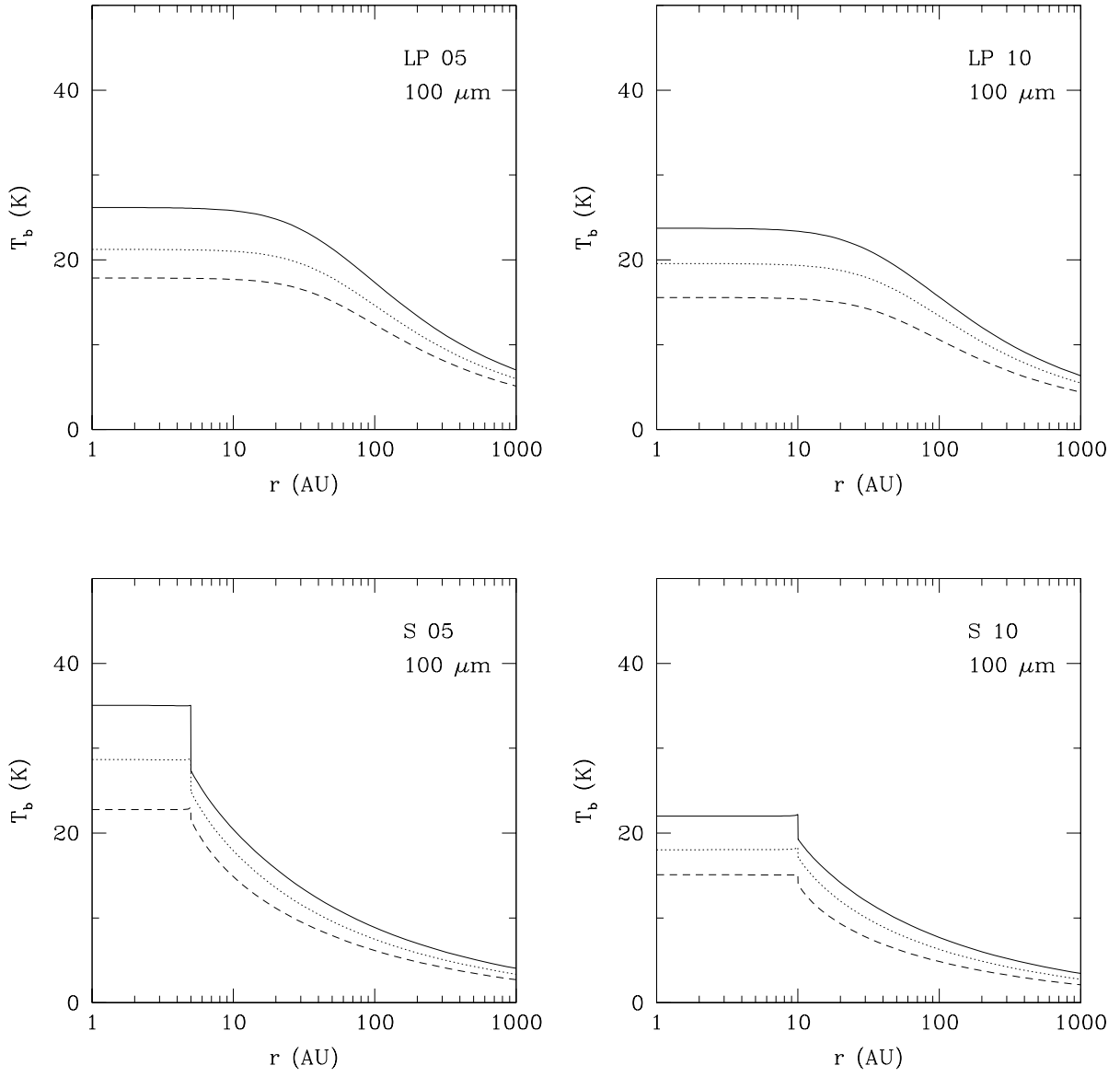


Fig. 18. The same as Figure 15 but for the observing wavelength at $100\mu\text{m}$ (frequency at 3THz).